

Surface and electronic structure of SmB_6 through Scanning Tunneling Microscopy

S. Rößler,¹ Lin Jiao,¹ D. J. Kim,² S. Seiro,¹ K. Rasim,¹ F. Steglich,¹ L. H. Tjeng,¹ Z. Fisk,² and S. Wirth^{1,*}

¹*Max Planck Institute for Chemical Physics of Solids, 01187 Dresden, Germany*

²*Department of Physics and Astronomy, University of California, Irvine, CA 92697*

(Dated: June 24, 2021)

SmB_6 , a so called Kondo insulator, is recently discussed as a candidate material for a strong topological insulator. We present detailed atomically resolved topographic information on the (001) surface from more than a dozen SmB_6 samples. Atomically flat, *in situ* cleaved surfaces often exhibit B- and Sm-terminated surfaces as well as reconstructed and non-reconstructed areas *coexisting* on different length scales. The terminations are unambiguously identified. In addition, electronic inhomogeneities are observed which likely result from the polar nature of the (001) surface and may indicate an inhomogeneous Sm valence at the surface of SmB_6 . In addition, atomically resolved topographies on a (110) surface are discussed.

I. INTRODUCTION

Topologically non-trivial surface states have evolved into a highly topical and active field of research. Here, the interest stems not only from the physics involved [1] but also from some of the unusual transport properties of the electrons within the surface states which render them attractive for potential applications [2]. The main idea relies on a sufficiently strong spin-orbit coupling in a bulk insulator which can result in topologically protected (by time-reversal symmetry) surface states [3, 4]. To this end, the product of the parity of all involved bands at the time reversal invariant momentum points is required to be -1 . In a seminal paper it was demonstrated that such conditions could be fulfilled in strongly correlated $4f$ systems in which a hybridization between conducting d -bands and localized f -bands takes place [5]. Here, the so-called Kondo insulators [6, 7] are of particular interest since they are characterized by a narrow gap and strong spin-orbit coupling. Subsequent band structure calculations for the well-known Kondo insulator SmB_6 indeed predicted non-trivial surface states [8–11]. It also sparked a flurry of experiments. Transport measurements were able to show that there is surface conductance [12–14]. A number of angle-resolved photoemission spectroscopy (ARPES) studies were conducted in an effort to provide support to the claim that these surface states are in fact topological in nature. In particular, results of spin-resolved ARPES were interpreted as evidence for the latter [15, 16]. However, other views have also been put forward including the involvement of a surface reconstruction and of the polar nature of the (001) SmB_6 surface [17, 18]. In addition, ARPES results down to 1 K have been discussed in terms of Rashba splitting [19].

One severe obstacle in resolving the afore-mentioned issues is the complexity of the SmB_6 surfaces, even if they are cleaved *in situ* and smooth down to an atomic level. We apply Scanning Tunneling Microscopy (STM) and Spectroscopy (STS) to provide information on the atomic length scale to show the multitude of different terminations often coexisting on the same surface. Atomically resolved spectroscopic data indicate electronic inhomogeneities on non-reconstructed surfaces. In addition, signatures of the Kondo effect being at play are presented.

II. EXPERIMENTAL

Single crystals of SmB_6 were synthesized by using an Al flux method [14]. The STM/STS work was conducted mostly in a low-temperature (LT) STM (base temperature 4.6 K, Omicron Nanotechnology) with ultra-high vacuum (UHV) of $p \leq 3 \times 10^{-9}$ Pa. Also, a UHV cryogenic STM was employed providing a base temperature of 0.3 K and a magnetic field of up to 12 T. The SmB_6 single crystals were cleaved *in situ* of the respective STM chamber and at temperatures of about 20 K. We report results on a total of 18 cleaves. Tunneling spectroscopy was measured by using a lock-in technique with small bias modulation (V_{mod}) at 117 Hz. If not stated otherwise, topographic images shown in the following were obtained at temperatures $T \sim 5$ K.

* Email: wirth@cpfs.mpg.de

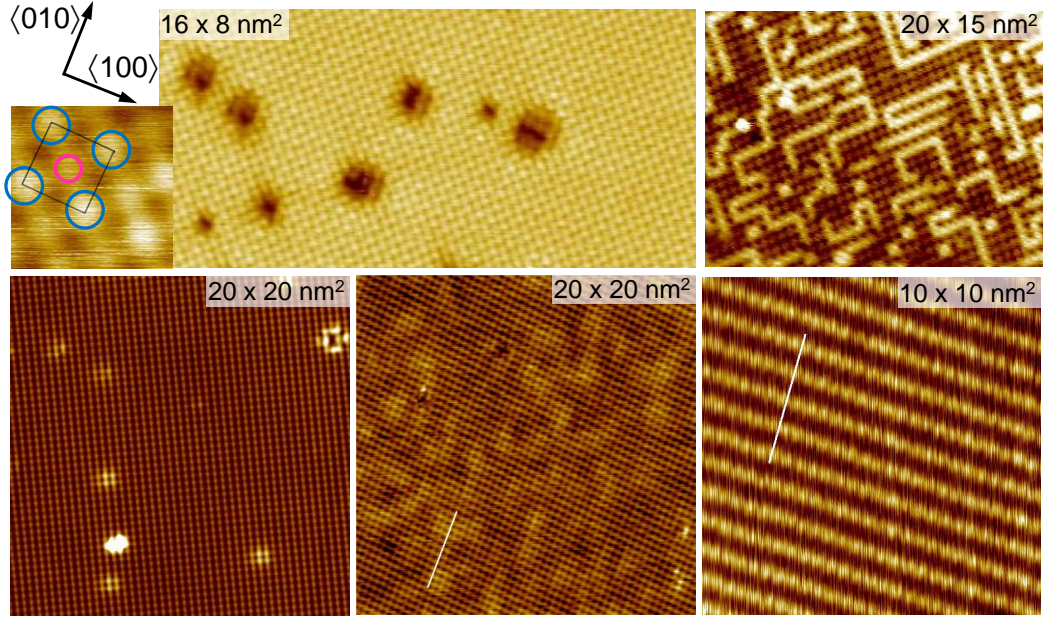


FIG. 1. Overview of the different topographies encountered for $\{001\}$ planes. The upper left and center topographies present Sm-terminated surfaces; the main crystallographic directions are indicated. The zoom on the left shows an area of $1 \times 1 \text{ nm}^2$, with the Sm (blue) and B (pink) apex atoms marked by circles [20]; cf. figure 2 for the crystal structure. The bottom left and center topographies exhibit B-termination; the center one adumbrates electronic inhomogeneity. The two images on the right depict reconstructed surfaces; the upper one disordered, the lower one ordered (2×1 reconstruction). White lines indicate a main crystallographic direction.

III. SURFACE TOPOGRAPHY, $\{001\}$ CRYSTALLOGRAPHIC PLANES

A. Overview

In figure 1 an overview of the different surfaces encountered so far is presented. It should be emphasized that these different topographies may come in various sizes (they can be as small as a few nm) and may coexist on one and the same surface depending on the investigated location. In STS, spectroscopy can be conducted on a well defined topography while measurements in which a certain area is investigated (e.g. ARPES, optical conductivity or point contact measurements) may very well average over different terminations with unknown weight. The upper central image of figure 1 presents a Sm-terminated surface. This can most easily be recognized by considering the main crystallographic directions (shown on the left side): the lines of corrugations run along the diagonal. This is obvious from the zoom on the left [20] which shows an area of $1 \times 1 \text{ nm}^2$. The Sm atoms (blue circles) exhibit the expected square arrangement along the main crystallographic directions and with correct distances (SmB_6 : cubic crystal structure with lattice constant $a = 4.133 \text{ \AA}$, cf. figure 2). In addition, also the apex of the B octahedra (pink) is clearly seen in the topography (the assignment of the atoms will become clear below). Very similar surface structures were observed on SmB_6 [21] as well as LaB_6 [22]. In contrast, the two topographies at bottom left and center depict B-terminated areas. Here, the corrugations are aligned parallel to the $\langle 100 \rangle$ directions (indicated by a white line in the center image). However, the center image clearly shows some underlying inhomogeneities (also seen in [23]) which are *not* present in the left image. We consider this inhomogeneity to be electronic in origin and discussed this below. The two images on the right visualize differently reconstructed surfaces. The upper one shows that the Sm atoms on top of the B surface do not necessarily need to order into a (2×1) reconstruction as it is presented in the lower image (for further discussion, see section III C). Some of the surface terminations reported here have also been observed by others [21, 23]. It should be noted, however, that all these smooth terminations need often to be searched for, while many areas appear rough on an atomic scale.

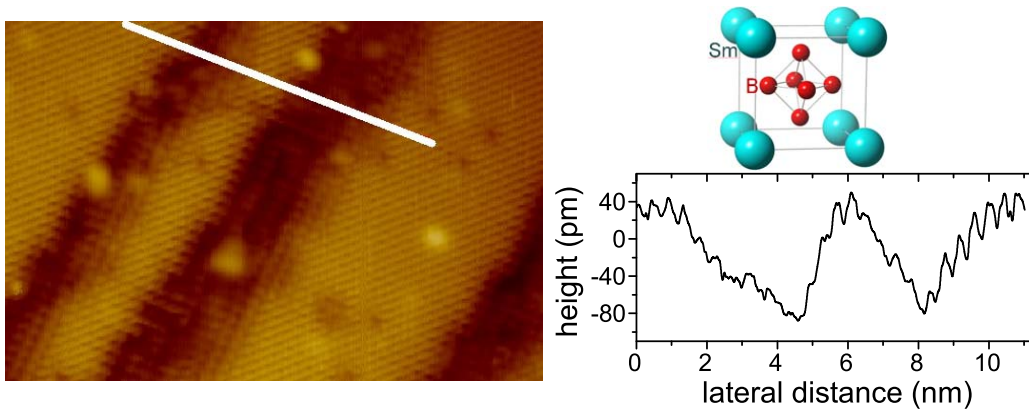


FIG. 2. Left: Example of non-reconstructed surface ($12 \times 18 \text{ nm}^2$) showing several steps between Sm- and B-terminated areas; bias voltage $V_b = 0.2 \text{ V}$, set point current $I_{sp} = 0.6 \text{ nA}$. The white line is almost parallel to a $\langle 100 \rangle$ crystallographic direction. Right: Height scan along the white line marked in the topography image. The cubic crystal structure of SmB_6 is also shown.

B. Assignment of the surface termination

In all discussions about the different surfaces it is pivotal to assign the termination properly, i.e. to unambiguously distinguish Sm- from B-termination. The likely most reliable way to achieve this is by the observation of atomically resolved steps separating different terminations, and specifically if these step heights are in agreement with expectations from the crystal structure [20]. Here, further support to this assignment is presented; this time by considering steps between alternating surface terminations as presented in the topography figure 2, left. In this $12 \times 18 \text{ nm}^2$ field of view, three “trenches” of approximately 100 pm in depth can clearly be made out, see height scan (figure 2, right) along the white line marked in the topographic image. Note that this height scan was taken almost parallel to one of the main crystallographic directions, i.e. along $\langle 100 \rangle$. We assign the upper (brighter in figure 2, left) terraces to Sm-terminated areas and the lower (darker) ones to B terminations for the following two reasons: i) The height difference of the upper and lower terraces corresponds approximately to the distance between the center of a B atom and the plane spanned by the four closest Sm atoms, i.e. half the distance of two *inter*-octahedral borons (0.083 nm). Of course, the heights as measured by STM are also influenced by the local density of states (DOS) and possibly also by some relaxation of the surface atom distances with respect to their bulk distances. Nonetheless, the measured heights are difficult to explain for any other assumed surface configuration. ii) As already seen for the non-reconstructed surfaces in figure 1, the corrugations on the upper terraces run along lines parallel to $\langle 110 \rangle$ (note that the white line in figure 2, left is almost parallel to $\langle 100 \rangle$). These corrugations have slightly alternating heights corresponding to an alternating visualization of Sm and B atoms with distances of $\approx \frac{1}{2}\sqrt{2}a$ along the diagonal [20]. In contrast, the corrugations within the lower areas of figure 2 are oriented along $\langle 100 \rangle$ with distances of a as expected if apex atoms of the B octahedra are visualized.

Within the cubic crystal structure of SmB_6 , the octahedra form sturdy B_6^{2-} polymeric anions. Yet, the *inter*-octahedral B-distance (0.1669 nm) is slightly smaller than the *intra*-octahedral distance (0.1744 nm) [24]. Hence, one might consider cleaving through the B_6 octahedra rather than between them. Indeed, we rarely observed “doughnut-shaped” structures (see figure 3(h)), similar to those reported in [21]. These “doughnuts” have diameters of about one lattice constant and therefore, are likely made up by eight boron atoms, i.e. two respective atoms out of each of four adjacent octahedra, cf. figure 2 for the SmB_6 unit cell and [21]. In order to rationalize the experimental findings, i.e. compare cleaving by breaking inter-octahedral vs. intra-octahedral bonds, electronic structure calculations with respect to the surface energies γ of differently terminated slabs were carried out. Density functional theory calculations in the generalized gradient approximation (GGA) were conducted for LaB_6 and CaB_6 , i.e. two hexaborides with integer valence La^{3+} and Ca^{2+} next to the intermediate valence $\nu \sim 2.6$ of SmB_6 . The implementation in the all-electron first principles code FHI-AIMS was employed using localized, numerically tabulated atom-centered orbitals [25]. For LaB_6 the calculated values are in good agreement with [26]: an energetic preference of the surface formed by cutting the inter-octahedral boron bonds ($\gamma = 2.97 \text{ Jm}^{-2}$), as compared to surfaces that cut intra-octahedral bonds ($\gamma = 3.62 \text{ Jm}^{-2}$), was found. For the case of CaB_6 , the difference is somewhat larger (2.77 Jm^{-2} and 3.92 Jm^{-2} , respectively). Surface relaxations do not yield substantial changes and decrease all mentioned surface energies by 0.1–0.2 Jm^{-2} . Assuming that qualitatively the same picture holds for SmB_6 , the calculations support the assertion above that in rare cases, e.g. in concert with respective lattice imperfections, the cleavage can also take place between intra-octahedral

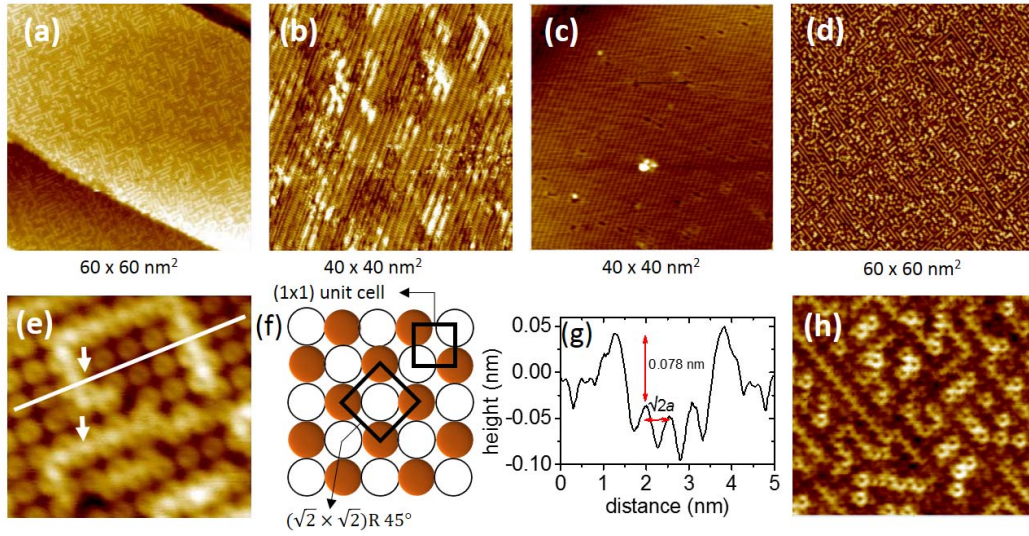


FIG. 3. (a)-(d) STM images of cleaved $\{001\}$ surface of SmB_6 . While (a), (b), and (d) are disordered, an ordered (2×1) reconstruction can be recognized in (c). (e) High resolution image ($5 \times 5 \text{ nm}^2$) of a disordered surface similar to (a), where Sm atoms form a self-organized labyrinth on top of a $(\sqrt{2} \times \sqrt{2})\text{R}45^\circ$ reconstructed B-terminated surface. Notice that across the Sm chains B_6 octahedra are anti-phase with each other (for example, see white arrows). (f) Schematic diagram of a $(\sqrt{2} \times \sqrt{2})\text{R}45^\circ$ reconstructed B-terminated surface. Empty black (solid brown) circles represent missing (filled) B_6 octahedra. (g) Line scan along the white line in (e). (h) High resolution zoomed ($10 \times 10 \text{ nm}^2$) image of (d) displaying doughnut-like features.

bonds, while in the *typical* case the cleaving is expected to leave the B octahedra intact.

The surface structure of figure 2 can be compared to the (2×1) reconstructed surface (figure 1 lower right): In both cases, Sm and B terminated surfaces are exposed simultaneously but on different length scales. Yet, tunneling spectra obtained on reconstructed surfaces clearly differ from those on non-reconstructed ones [20, 23]. This again emphasizes the need for detailed *local* information on the exact surface structure.

C. Atomically reconstructed surfaces

As already mentioned, a bulk truncated $\{001\}$ surface of SmB_6 is polar due to uncompensated charges at the surface. The intermediate valence of Sm renders a simple electron counting even more complicated. However, several reasons may give rise to complex surface morphologies, such as a concomitant reduction of the free energy [27] and/or an accommodation of the strain induced by the atomic size mismatch of the constituents [28]. In consequence, a variety of differently reconstructed surfaces was reported based on atomically resolved STM [20, 21, 23]. In figure 3(a)-(d), the STM images of $\{001\}$ surfaces on areas as large as $60 \times 60 \text{ nm}^2$ are presented. Such atomically reconstructed regions can extend up to a few microns. A single cleave at low temperatures can produce all these different types of topographies indicating that they all lie close in energy. The topographic images in figures 3(a), (b) and (d) are disordered, whereas (c) displays an ordered (2×1) reconstruction (cf. also figure 1 right). The latter type of reconstruction was observed previously in STM and low-energy electron diffraction (LEED) measurements [29, 30].

The surface displayed in figure 3(a) is particularly interesting: Here, Sm atoms form a self-organized labyrinth-like structure on a $(\sqrt{2} \times \sqrt{2})\text{R}45^\circ$ reconstructed B-terminated surface. In figure 3(e), a high resolution image of a similar surface is presented. Across the Sm-chain, the B_6 octahedra are shifted by half a unit cell, i.e., they are anti-phase with respect to each other. In figure 3(f) a schematic diagram of such a $(\sqrt{2} \times \sqrt{2})\text{R}45^\circ$ reconstruction is presented, in which the missing B_6 octahedra are represented by black circles. These reconstructions are also found in the mixed-valent material Fe_3O_4 [31]. A height scan along the white line in figure 3(e) can be seen in figure 3(g). The Sm-Sm valley-height with respect to that of B_6 - B_6 is found to be 0.078 nm, which is comparable to the distance of 0.083 nm between the top B-atom of the B_6 octahedra and the plane made up by the four closest Sm atoms in the SmB_6 unit cell (i.e., half the inter-octahedra distance). Further, the B_6 - B_6 distance 0.56 nm is close to $\sqrt{2}a$, which is consistent with a $(\sqrt{2} \times \sqrt{2})\text{R}45^\circ$ -type reconstruction. Figure 3(h) depicts a high resolution zoom-in image of (d). This disordered surface is likely comprised of both Sm as well as B atoms. Similar doughnut-like features have been reported in [21].

It is needless to mention that the surface reconstructions may easily result in even more complex surface states,

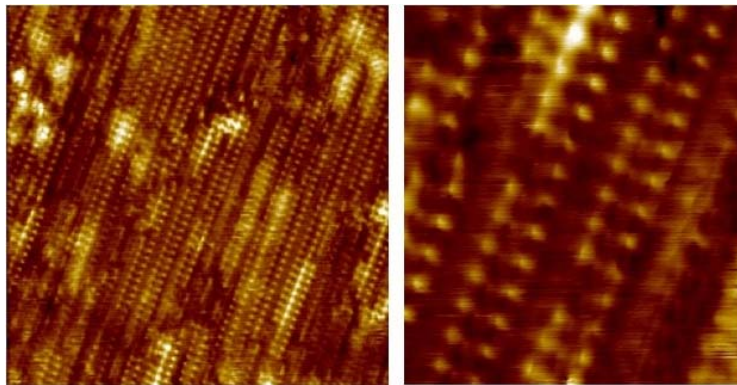


FIG. 4. STM images of a cleaved $\{110\}$ surface of SmB_6 ; left: $20 \times 20 \text{ nm}^2$, right: $4 \times 5 \text{ nm}^2$; $V_b = 0.2 \text{ V}$, $I_{sp} = 0.6 \text{ nA}$. Although atomic corrugations can clearly be recognized, these surfaces are not as smooth as those obtained for $\{001\}$ planes.

which make a straightforward observation of the topologically non-trivial surface states an experimental challenge. A well-known example for the formation of a metallic surface layer is the $\text{Si}(111)7 \times 7$ reconstruction [32].

IV. SURFACES ALONG THE $\{110\}$ PLANE

In contrast to the $\{100\}$ surface discussed in section III, the $\{110\}$ surface of SmB_6 is *not* polar. Hence, one could expect that an interpretation of results obtained on the latter is more straightforward. For the $\{110\}$ surface, two additional surface Dirac points were predicted [33]. Also, experimental results obtained on cleaved $\{110\}$ surfaces have been reported [34, 35].

Different areas of a cleaved $\{110\}$ surface are presented in figure 4. Clearly, atomic resolution is achieved and the rectangular arrangement expected for Sm atoms on a $\{110\}$ plane with correct distances is seen in the zoomed-in image. However, the surfaces appear certainly not as smooth as those obtained on $\{001\}$ surfaces, contain numerous defects and therefore, likely, different types of atoms and may exhibit locally varying atomic environments. Consequently, care has to be taken in interpreting spectroscopic results unless the quality of the surfaces is improved.

V. ELECTRONIC INHOMOGENEITIES AT THE SURFACE

In the following we focus on $\{001\}$ surfaces which are not atomically reconstructed. Spectroscopy on smaller (a few nm in extent) non-reconstructed areas revealed indications for the hybridization gap [20] expected for a Kondo insulator at low temperatures. In contrast, on larger areas—at least several tens of nm in extent—the tunneling spectral line-shape typically appeared as a Fano resonance [36], owing to a quantum mechanical interference of the electrons tunneling from (to) the STM tip into (out of) the quasiparticle states and the conduction band. Then, the tunneling conductance $g(V) = dI(V)/dV$ can be fitted by [37]

$$g(V) \propto \frac{(\epsilon + q)^2}{\epsilon^2 + 1}, \quad \epsilon = \frac{2(eV - E_0)}{\Gamma}. \quad (1)$$

Here, Γ and E_0 are the width of the resonance and its position in energy, respectively. The asymmetry parameter q is determined by the probabilities of tunneling into the quasiparticle states and the conduction band, as well as by the particle-hole asymmetry [38]. Although the bare local DOS of SmB_6 is obscured by the Fano resonance, the parameter Γ can be related to the Kondo temperature T_K [39].

The STM topography, as shown in figure 5(a), was conducted on an area of $10 \times 10 \text{ nm}^2$ in a dual bias mode. This implies that the same area can be scanned with two different bias voltages applied for the forward and backward scans. In the present case, the forward scan was conducted with $V_b = +0.025 \text{ V}$, figure 5(a), while $V_b = -0.025 \text{ V}$ was used for the backward scan in figure 5(b). The fact that exactly the same areas were visualized is evidenced by the impurity marked by the white circles in figures 5(a) and (b). Nonetheless, a strong spatial inhomogeneity is seen in figure 5(b), which is not present in figure 5(a). Since the tunneling conductance is a convolution of tip-sample distance and the local DOS, this suggests not only a spatially inhomogeneous but also an asymmetric local DOS with respect to the sign of V_b . This can be more clearly inferred from the tunneling conductance presented in figures 5(c).

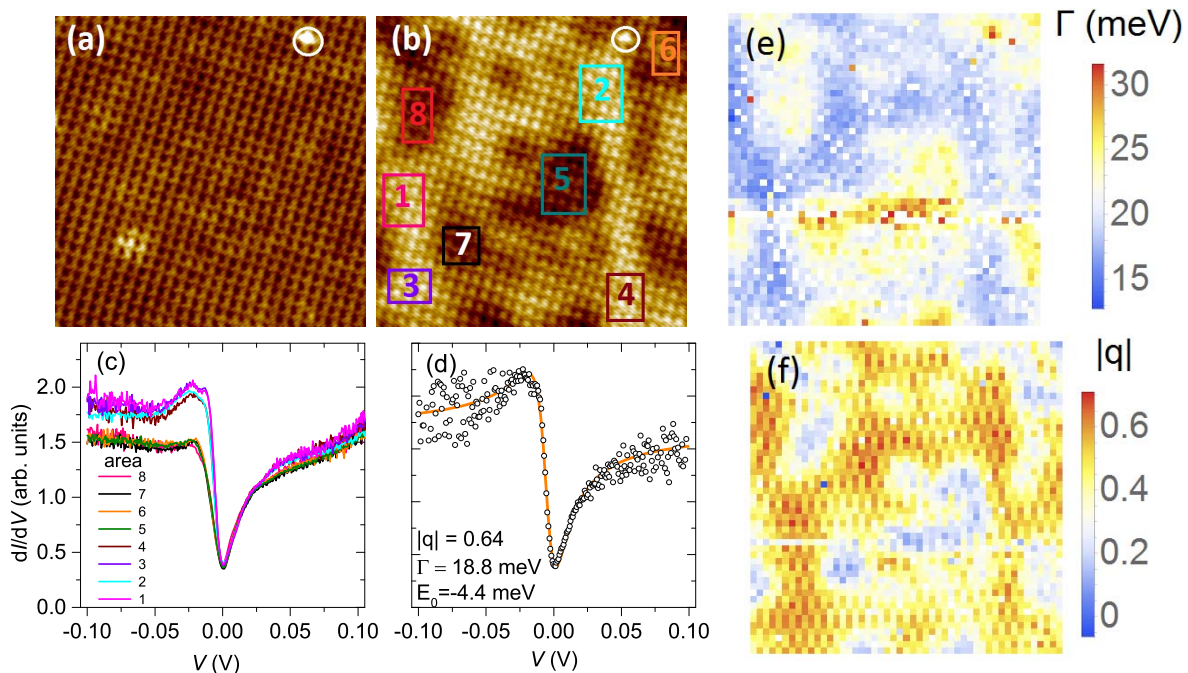


FIG. 5. Topography of SmB_6 over an area of $10 \times 10 \text{ nm}^2$ measured at 6 K using a dual bias mode: (a) Forward scan with $V_b = +0.025 \text{ V}$ and (b) backward scan with $V_b = -0.025 \text{ V}$. An impurity marked by white circles confirms that both images were taken on the same area. (c) Average tunneling conductance $g(V)$ on areas marked by matching colors in (b). (d) Typical single tunneling spectrum and corresponding fit (continuous line) to Equation 1. (e) and (f) Spatial variation of Γ and $|q|$, respectively.

Here, the dI/dV -curves were obtained by averaging over the areas shown in (b) with matching colors. These curves differ significantly between $-0.2 \gtrsim V_b < 0 \text{ mV}$. A fit of all 2500 individual spectra obtained within the field of view of figures 5(a) and (b) were fitted to Equation 1; an example is given in figure 5(d). The resulting spatial maps for Γ and $|q|$ are presented in figures 5(e) and (f), respectively. Notably, Γ and $|q|$ are anti-correlated, i.e., the regions with larger values of Γ exhibit smaller values of $|q|$. This is consistent since larger values of Γ suggest stronger hybridization. Because the hybridization in SmB_6 takes place between $\text{Sm } 4f$ states and the $5d$ conduction band, a large Γ may implies that the $5d$ bands are more occupied, which in turn can give rise to a higher probability of tunneling into the conduction band, i.e. smaller $|q|$. We speculate that the spatial inhomogeneities of Γ and $|q|$ is related to a spatially inhomogeneous intermediate valence of Sm at the surface of SmB_6 .

Within our field of view, E_0 is found to vary between $-7 \text{ meV} < E_0 < 1 \text{ meV}$, with a pronounced maximum of probability at $E_0 \approx -3.8 \text{ meV}$. Since the hybridization gap in SmB_6 is about 15–20 meV [13, 20, 40, 41], one may assume that the Fano resonance found here is likely a phenomenon related to the in-gap states lying close to the Fermi level E_F . As mentioned above, in order for the Fano resonance to show up, two types of tunneling channels are required. One may then speculate about the two contributions changing locally, i.e. the heavy quasiparticles related to the bulk and the conduction band being related to the surface states, both of which residing inside the hybridization gap. Evidence for the former is found in specific heat [42] and recent ARPES measurements [19]. The latter have been detected in the de Haas-van Alphen (dHvA) experiments, which report two dimensional Fermi surfaces with light effective mass of the quasiparticles [43].

VI. KONDO EFFECT

As mentioned above, SmB_6 is an intermediate-valence compound with a Sm valence of $\nu \approx 2.6$ [44]. For such a value of ν it is questionable to what extent the standard Kondo picture can be applied [45].

In figure 6 left, the susceptibility is recapped for one of our samples. In line with earlier measurements [7, 13, 46] it exhibits Curie-Weiss-like and van Vleck contributions (due to its intermediate valence) for $T \gtrsim 100 \text{ K}$, and non-magnetic behavior with an enlarged DOS at E_F at lowest temperatures.

Whether or not such a behavior is related to an underlying Kondo effect has been discussed controversially, see

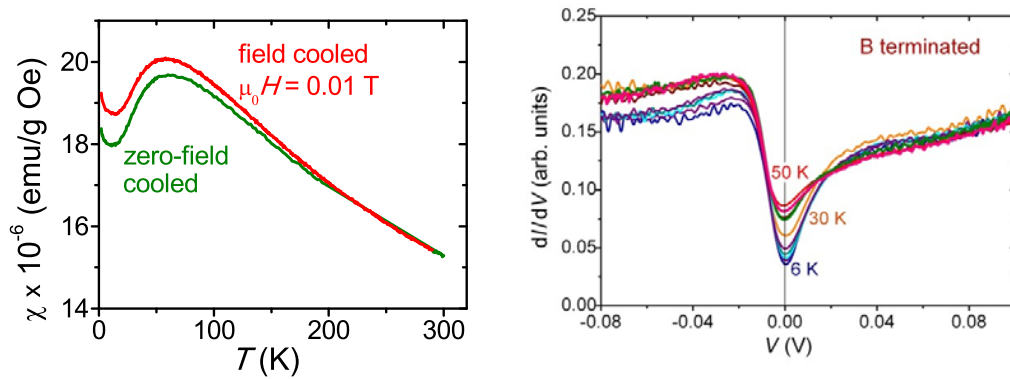


FIG. 6. Left: Temperature dependence of the susceptibility χ . Right: Tunneling spectra on a B-terminated surface of SmB_6 at temperatures $6 \text{ K} \leq T \leq 50 \text{ K}$ clearly showing Fano-type line-shapes and a closing-up of the partial gap at zero-bias with increasing T .

e.g. [6, 7, 47–49]. More recent support for the Kondo picture was provided e.g. by the analysis of point contact measurements [13]. The closing-up of the gap as observed by temperature dependent STS measurements on small, non-reconstructed surface areas was also consistent with expectations for the Kondo effect [20]. In figure 6 right, $g(V)$ -spectra obtained on a large, non-reconstructed B-terminated area in the range $6 \text{ K} \leq T \leq 50 \text{ K}$ is presented. In contrast to [20], the spectra here are clearly of Fano-type. Yet, the closing of the (partial) gap with increasing temperature follows the same trend and hence, is again consistent with a logarithmic behavior expected for the Kondo effect [50]. Note that very similar Fano line-shapes were obtained on a (2×1) reconstructed surface in the temperature range $8 \text{ K} \leq T \leq 30 \text{ K}$ and the respective spectra were interpreted in terms of hybridization resulting from the underlying Kondo lattice [23].

ACKNOWLEDGEMENTS

The authors gratefully acknowledge experimental help by Tae-Hwan Jang and insightful discussions with Yuri Grin. Work at UC Irvine is supported by the Defense Advanced Research Agency (DARPA) under agreement number FA8650-13-1-7374.

-
- [1] M.Z. Hasan and C.L. Kane, Rev. Mod. Phys. **82** (2010) 3045.
 - [2] A. Stern, D.K. Efimkin, V. Galitski, J. Xia and Z. Fisk, arXiv:1510.02569.
 - [3] C.L. Kane and E.J. Mele, Phys. Rev. Lett. **95** (2005) 146802.
 - [4] L. Fu and C.L. Kane, Phys. Rev. B **76** (2007) 045302.
 - [5] M. Dzero, K. Sun, V. Galitski and P. Coleman, Phys. Rev. Lett. **104** (2010) 106408.
 - [6] G. Aeppli and Z. Fisk, Comments Cond. Mat. Phys. **16** (1992) 155.
 - [7] P.S. Riseborough, Adv. Phys. **49** (2000) 257.
 - [8] T. Takimoto, J. Phys. Soc. Jpn. **80** (2011) 123710.
 - [9] F. Lu, J.Z. Zhao, H. Weng, Z. Fang and X. Dai, Phys. Rev. Lett. **110** (2013) 096401.
 - [10] V. Alexandrov, M. Dzero and P. Coleman, Phys. Rev. Lett. **111** (2013) 226403.
 - [11] J. Kim, K. Kim, C.-J. Kang, S. Kim, H.C. Choi, J.-S. Kang, J.D. Denlinger and B.I. Min, Phys. Rev. B **90** (2014) 075131.
 - [12] S. Wolgast, C. Kurdak, K. Sun, J.W. Allen, D.J. Kim and Z. Fisk, Phys. Rev. B **88** (2013) 180405(R).
 - [13] X. Zhang, N.P. Butch, P. Syers, S. Ziemak, R.L. Greene and J. Paglione, Phys. Rev. X **3** (2013) 011011.
 - [14] D.-J. Kim, S. Thomas, T. Grant, J. Botimer, Z. Fisk and J. Xia, Sci. Rep. **3** (2013) 3150.
 - [15] N. Xu, P.K. Biswas, J.H. Dil, R.S. Dhaka, G. Landolt, S. Muff, C.E. Matt, X. Shi, N.C. Plumb, M. Radovic, E. Pomjakushina, K. Conder, A. Amato, S.V. Borisenko, R. Yu, H.-M. Weng, Z. Fang, X. Dai, J. Mesot, H. Ding and M. Shi, Nature Comm. **5** (2014) 4566.
 - [16] S. Suga, K. Sakamoto, T. Okuda, K. Miyamoto, K. Kuroda, A. Sekiyama, J. Yamaguchi, H. Fujiwara, A. Irizawa, T. Ito, S. Kimura, T. Balashov, W. Wulfhekel, S. Yeo, F. Iga, S. Imada, J. Phys. Soc. Jpn. **83** (2014) 014705.
 - [17] Z.-H. Zhu, A. Nicolaou, G. Levy, N.P. Butch, P. Syers, X.F. Wang, J. Paglione, G.A. Sawatzky, I.S. Elfimov and A. Damascelli, Phys. Rev. Lett. **111** (2013) 216402.

- [18] E. Frantzeskakis, N. de Jong, B. Zwartsenberg, Y.K. Huang, Y. Pan, X. Zhang, J.X. Zhang, F.X. Zhang, L.H. Bao, O. Tegus, A. Varykhalov, A. de Visser and M.S. Golden, *Phys. Rev. X* **3** (2013) 041024.
- [19] P. Hlawenka, K. Siemensmeyer, E. Weschke, A. Varykhalov, J. Sánchez-Barriga, N.Y. Shitsevalova, A.V. Dukhnenko, V.B. Filipov, S. Gabáni, K. Flachbart, O. Rader and E.D.L. Rienks, arXiv:1502.1542 (2015).
- [20] S. Rößler, T.-H. Jang, D.-J. Kim, L.H. Tjeng, Z. Fisk, F. Steglich and S. Wirth, *Proc. Natl. Acad. Sci. USA* **111** (2014) 4798.
- [21] W. Ruan, C. Ye, M. Guo, F. Chen, X. Chen, G.-M. Zhang and Y. Wang, *Phys. Rev. Lett.* **112** (2014) 136401.
- [22] J.S. Ozcomert and M. Trenary, *Surf. Sci. Lett.* **265** (1992) 227.
- [23] M.M. Yee, Yang He, A. Soumyanarayanan, D.-J. Kim, Z. Fisk, and J.E. Hoffman, arXiv:1308.1085 (2013).
- [24] I.D.R. Mackinnon, J.A. Alarco and P.C. Talbot, *Model. and Numer. Simul. of Mater. Sci.* **3** (2013) 158.
- [25] V. Blum, R. Gehrke, F. Hanke, P. Havu, V. Havu, X. Ren, K. Reuter and M. Scheffler, *Comp. Phys. Comm.* **180** (2009) 2175.
- [26] M.A. Uijttewaai, G.A. de Wijs and R.A. de Groot, *J. Phys. Chem. B* **110** (2006) 18459.
- [27] H. Röder, R. Shuster, H. Brune and K. Kern, *Phys. Rev. Lett.* **71** (1993) 2086.
- [28] J. Tersoff, *Phys. Rev. Lett.* **74** (1995) 434.
- [29] M. Aono, R. Nishitani, T. Tanaka, E. Bannai and S. Kawai, *Solid State Commun.* **28** (1978) 409.
- [30] H. Miyazaki, T. Hajiri, T. Ito, S. Kunii and S.-i. Kimura, *Phys. Rev. B* **86** (2012) 075105.
- [31] N. Stanka, W. Hebenstreit, U. Diebold, and S. A. Chambers, *Surf. Sci.* **448** (2000) 49.
- [32] K. Yoo and H.H. Weitering, *Phys. Rev. B* **65** (2002) 115424.
- [33] M. Ye, J.W. Allen and K. Sun, arXiv:1307.7191.
- [34] F. Chen, C. Shang, Z. Jin, D. Zhao, Y.P. Wu, Z.J. Xiang, Z.C. Xia, A.F. Wang, X.G. Luo, T. Wu and X.H. Chen, *Phys. Rev. B* **91** (2015) 205133.
- [35] B.S. Tan, Y.-T. Hsu, B. Zeng, M.C. Hatnean, N. Harrison, Z. Zhu, M. Hartstein, M. Kiourlappou, A. Srivastava, M.D. Johannes, T.P. Murphy, J.-H. Park, L. Balicas, G.G. Lonzarich, G. Balakrishnan and S.E. Sebastian, *Science* **349** (2015) 287.
- [36] U. Fano, *Phys. Rev.* **124** (1961) 1866.
- [37] A. Schiller and S. Hershfield, *Phys. Rev. B* **61** (2000) 9036.
- [38] J. Figgins and D.K. Morr, *Phys. Rev. Lett.* **104** (2010) 187202.
- [39] K. Nagaoka, T. Jamneala, M. Grobis and M.F. Crommie, *Phys. Rev. Lett.* **88** (2002) 077205.
- [40] B. Gorshunov, N. Sluchanko, A. Volkov, M. Dressel, G. Knebel and A. Loidl, *Phys. Rev. B* **59** (1999) 1808.
- [41] M. Neupane, N. Alidoust, S.-Y. Xu, T. Kondo, Y. Ishida, D.-J. Kim, C. Liu, I. Belopolski, Y.J. Jo, T.-R. Chang, H.-T. Jeng, T. Durakiewicz, L. Balicas, H. Lin, A. Bansil, S. Shin, Z. Fisk and M.Z. Hasan, *Nature Commun.* **4** (2013) 2991.
- [42] S. Gabáni, K. Flachbart, E. Konovalova, M. Orendáč, Y. Paderno, V. Pavlík and J. Šebek, *Solid State Commun.* **117** (2001) 641.
- [43] G. Li, Z. Xiang, F. Yu, T. Asaba, B. Lawson, P. Cai, C. Tinsman, A. Berkley, S. Wolgast, Y.S. Eo, D.-J. Kim, C. Kurdak, J.W. Allen, K. Sun, X.H. Chen, Y.Y. Wang, Z. Fisk and Lu Li, *Science* **346** (2014) 1208.
- [44] M. Mizumaki, S. Tsutsui and F. Iga, *J. Phys.: Conf. Series* **176** (2009) 12034.
- [45] C. M. Varma, *Phys. Rev. B* **50** (1994) 9952.
- [46] S. Gabáni, K. Flachbart, V. Pavlík, T. Herrmannsdörfer, E. Konovalova, Y. Paderno, J. Briančin and J. Trpčevská, *Czech. J. Phys.* **52** (2002) A225.
- [47] J.C. Cooley, M.C. Aronson, Z. Fisk and P.C. Canfield, *Phys. Rev. Lett.* **74** (1995) 1629.
- [48] B.R. Coles, *Physica B* **230-232** (1997) 718.
- [49] T. Kasuya, *J. Phys. Soc. Jpn.* **65** (1996) 2548.
- [50] T.A. Costi, *Phys. Rev. Lett.* **85** (2000) 1504.